Research Article

Stephen D. Hsu* and Jingjing Liu

Challenges of anamorphic high-NA lithography and mask making

Abstract: Chip makers are actively working on the adoption of 0.33 numerical aperture (NA) EUV scanners for the 7-nm and 5-nm nodes (B. Turko, S. L. Carson, A. Lio, T. Liang, M. Phillips, et al., in 'Proc. SPIE9776, Extreme Ultraviolet (EUV) Lithography VII', vol. 977602 (2016) doi: 10.1117/12.2225014; A. Lio, in 'Proc. SPIE9776, Extreme Ultraviolet (EUV) Lithography VII', vol. 97760V (2016) doi: 10.1117/12.2225017). In the meantime, leading foundries and integrated device manufacturers are starting to investigate patterning options beyond the 5-nm node (O. Wood, S. Raghunathan, P. Mangat, V. Philipsen, V. Luong, et al., in 'Proc. SPIE. 9422, Extreme Ultraviolet (EUV) Lithography VI', vol. 94220I (2015) doi: 10.1117/12.2085022). To minimize the cost and process complexity of multiple patterning beyond the 5-nm node, EUV high-NA single-exposure patterning is a preferred method over EUV double patterning (O. Wood, S. Raghunathan, P. Mangat, V. Philipsen, V. Luong, et al., in 'Proc. SPIE. 9422, Extreme Ultraviolet (EUV) Lithography VI', vol. 94220I (2015) doi: 10.1117/12.2085022; J. van Schoot, K. van Ingen Schenau, G. Bottiglieri, K. Troost, J. Zimmerman, et al., 'Proc. SPIE. 9776, Extreme Ultraviolet (EUV) Lithography VII', vol. 97761I (2016) doi: 10.1117/12.2220150). The EUV high-NA scanner equipped with a projection lens of 0.55 NA is designed to support resolutions below 10 nm. The high-NA system is beneficial for enhancing resolution, minimizing mask proximity correction bias, improving normalized image log slope (NILS), and controlling CD uniformity (CDU). However, increasing NA from 0.33 to 0.55 reduces the depth of focus (DOF) significantly. Therefore, the source mask optimization (SMO) with sub-resolution assist features (SRAFs) are needed to increase DOF to meet the demanding full chip process control requirements (S. Hsu, R. Howell, J. Jia, H.-Y. Liu, K. Gronlund, et al., EUV 'Proc. SPIE9048, Extreme Ultraviolet (EUV) Lithography VI', (2015) doi: 10.1117/12.2086074). To ensure no assist feature printing, the assist feature sizes need to be scaled with λ/NA. The extremely small SRAF width (below 25 nm on the reticle) is difficult to fabricate across the full reticle. In this paper, we introduce an innovative 'attenuated SRAF' to improve SRAF manufacturability and still maintain the process window benefit. A new mask fabrication process is proposed to use existing mask-making capability to manufacture the attenuated SRAFs. The high-NA EUV system utilizes anamorphic reduction; 4× in the horizontal (slit) direction and 8× in the vertical (scanning) direction (J. van Schoot, K. van Ingen Schenau, G. Bottiglieri, K. Troost, J. Zimmerman, et al., 'Proc. SPIE. 9776, Extreme Ultraviolet (EUV) Lithography VII', vol. 97761I (2016) doi: 10.1117/12.2220150; B. Kneer, S. Migura, W. Kaiser, J. T. Neumann, J. van Schoot, in 'Proc. SPIE9422, Extreme Ultraviolet (EUV) Lithography VI', vol. 94221G (2015) doi: 10.1117/12.2175488). For an anamorphic system, the magnification has an angular dependency, and thus, familiar mask specifications such as mask error factor (MEF) need to be redefined. Similarly, mask-manufacturing rule check (MRC) needs to consider feature orientation.

*Corresponding author: Stephen D. Hsu, Brion Technologies Inc., Brion, 399 West Trimble Road, San Jose, CA 95131, USA, e-mail: stephen.hsu@asml.com
Jingjing Liu: Brion Technologies Inc., Brion, 399 West Trimble Road, San Jose, CA 95131, USA

1 Introduction

The current state-of-the-art EUV scanner with 0.33 NA is able to support 13-nm half-pitch resolution [1, 2]. For sub-13-nm half-pitch resolution, lithographic patterning techniques such as multiple patterning and higher-NA imaging have been proposed as alternative options [3]. This paper focuses on using EUV high-NA imaging to achieve sub-13-nm half-pitch resolution, which is the most cost-effective

solution [4]. As NA increases from 0.33 to 0.55, the DOF decreases by 64% according to the Rayleigh criterion for depth of focus:

$$\text{DOF} = k_2 \frac{\lambda}{\text{NA}^2} \qquad (1)$$

where λ is the wavelength, and k_2 is a process-dependent constant. DOF reduction impacts the total focus budget for high-volume manufacturing (HVM) process control. Sub-resolution assist features (SRAFs) can improve the DOF [5]. However, as NA increases, the SRAF size also needs to be significantly reduced to avoid unwanted SRAF sidelobe printing. The SRAF size is a function of λ/NA. As the design rule half pitch is reduced to 20 nm, high-NA EUV systems require very small SRAFs, which are very challenging for mask making. Figure 1 shows the typical size of SRAFs along with the design rule minimum half pitch.

This paper is structured as follows: in Section 2 of this paper, we investigate both the advantages of the high-NA (0.55) EUV system and the challenges it poses, aiming to understand the magnitude of the effects. Section 3 describes how to use attenuated assist features to extend the compatibility of mask making with relaxed MRC. Section 4 pays specific attention to the design target (1×) and the conversion to anamorphic reticles for reticle manufacturing rule check, from both OPC and SRAF perspectives. Section 5 concludes with the main findings and new concepts introduced in the paper.
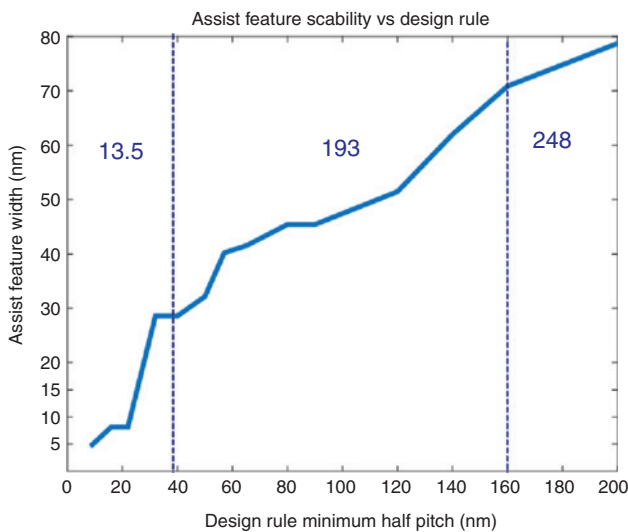

Figure 1: The typical size of SRAFs at 1× wafer level along with design rule minimum half pitch. As the design rule half pitch reduces down to 20 nm, high-NA EUV systems require extremely small SRAFs (<5 nm at 1×), which are beyond mask-writing capability according to the 2015 ITRS lithography roadmap.

2 The impact of EUV high-NA on lithography performance

To increase the NA in a reflective optical system, the angular spread at chief-ray-angle-at-object (CRAO) side must increase. For a 6° CRAO, the incoming and outgoing cones of light start to overlap with each other as NA increases beyond 0.4. Such optical systems cannot function properly [6]. The problem can be resolved by increasing the CRAO. However, EUV mirror coatings are not able to effectively reflect the combination of large angle and angular spread; thus, multilayer coatings can only handle a small range of angles, and the larger 'shadow' effect on the mask will result in reduced contrast and increased telecentricity error [7]. The incident angles and angular spread on the EUV optics and the reticle are reduced if the demagnification of the projection optics in the scanning direction is increased to 8×. Maintaining demagnification in the slit direction at 4× yields an anamorphic design for the EUV high-NA system with the imaging capability comparable to an isomorphic 8× system while maintaining good throughput [7].

Increasing the NA of a scanner generally improves the imaging resolution and reduces the proximity effect. For a 4× by 8× anamorphic system, vertical and horizontal spacings between the main features on the reticle is different, and the spacing between the horizontal features is twice as large as the spacing between the vertical features. Therefore, we are able to insert SRAFs, which subsequently affect the mask-manufacturing rule check (MRC). Section 4.2 gives a more detailed discussion of MRC impact. To systematically study the proximity behavior and imaging performance, we use four figures of merit: (1) the mask bias for printing wafer CD on target, (2) best focus shift of all features with respect to the overlapping process window, (3) normalized image log slope (NILS), and (4) CD uniformity (CDU) through defocus, dose, and mask error variation. CDU(3σ) calculation is defined in equation (2):

$$\text{CDU} = \frac{\sqrt{\text{CDR}_{\text{focus}}^2 + \text{CDR}_{\text{dose}}^2 + \text{CDR}_{\text{mask}}^2}}{2} \qquad (2)$$

where CDR refers to CD range (maxCD – minCD) over the specified process window conditions, and the denominator '2' is used to convert the CD range (6σ) to CD uniformity (3σ).

For the first part of the study, we focus on printing trenches through pitch using dark field mask. We select an annular illumination with inner σ = 0.5 and outer σ = 1.0 for NA = 0.55 and 0.33, and perform mask optimization without SRAFs using ASML Brion's Tachyon software

(ASML-Brion Inc., San Jose, CA, USA). To make a fair comparison, we select the design pitch such that both 0.55 NA and 0.33 NA have similar k_1 value ($k_1 \approx 0.4$). For 0.55 NA, the features are CD = 11 nm and pitch ranging from 20 nm to 150 nm. For 0.33 NA, the features are CD = 15 nm and pitch ranging from 30 nm to 150 nm. For both cases, the dose is anchored at the densest pitch without any anchor bias. To account for the resist blurring effect, for all imaging calculations, we convolve the aerial image with a 2-nm width Gaussian function. For CDU calculation, we use a window (PW) variation of ±5% of nominal exposure latitude, ±0.25 nm mask bias (at wafer scale), and a defocus value of half of the overlapping PW of all features. Figure 2A shows that the 0.55-NA system gives less CDU variation through pitch than the 0.33-NA system for both horizontal and vertical lines. In addition, for the 0.55-NA anamorphic system, the horizontal lines have a 16% lower CDU than the vertical lines. A major reason is that the 8× demagnification of the horizontal lines is twice as large as that of the vertical features; hence, it is easier to print and more robust to dose, focus, and mask error. Figure 2B shows that the mask bias to correct the CD to target is reduced for both lines at 0.55 NA as expected from the proximity effect of the higher-NA system. The same trend is observed in the best focus shift due to the reduced DOF of the higher-NA system; cf. Figure 2C. As

expected, Figure 2D indicates that the high-NA system offers improved NILS for both horizontal and vertical features compared with the NILS of the 0.33-NA system. Also, for the higher-NA system, the horizontal lines exhibit higher NILS than the vertical lines. The phenomenon of the best focus shift for different features is related to the electromagnetic field effects, which introduce a phase shift with respect to the thin mask. Burkhardt demonstrated that an optimized illumination design can flatten the Bossungs and, consequently, reduce CDU [8]. Therefore, a non-trivial co-optimization of the source and the mask is required.

For the second part of the study, we use ASML Brion's Tachyon source mask optimization (SMO) to co-optimize the source and mask without SRAFs. We focus on applying SMO to image the same features in the first part of the study with and without clear SRAFs on a dark field mask. For both 0.55 NA and 0.33 NA systems, the dose is anchored at the respective densest vertical pitch without any anchor bias optimization. For 0.55 NA systems, the central obscuration is set to 0.2 [6]. Figure 3 shows that by applying SMO CDU, the mask bias, and best focus shift are significantly reduced, and NILS is greatly improved compared with mask-only optimization for both 0.55 NA and 0.33 NA systems. As expected, the 0.55-NA tool maintains an advantage over the 0.33-NA tool for CDU, mask bias, and
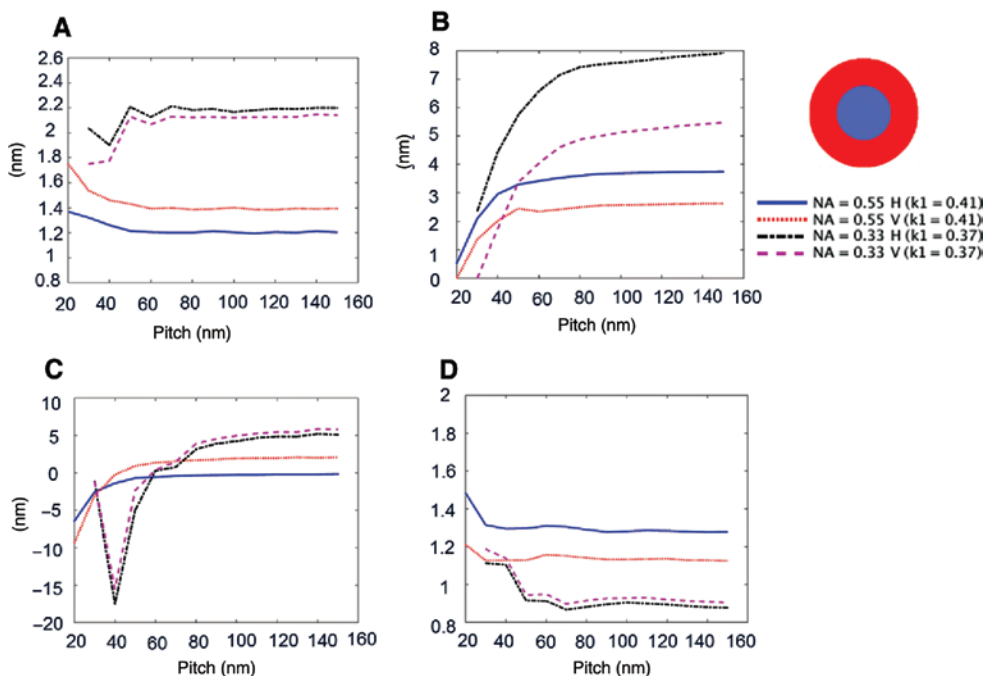

Figure 2: The CDU (A), mask bias (B), best focus shift (C), and NILS (D) for horizontal and vertical lines. The k_1 values for the 0.33 NA and 0.55 NA tools are approximately equal at minimum pitch. The source is an annular ring with inner σ = 0.5 and outer σ = 1.0. Line printing at 0.55 NA and 0.33 NA are anchored at the respective densest vertical pitch without any anchor bias.
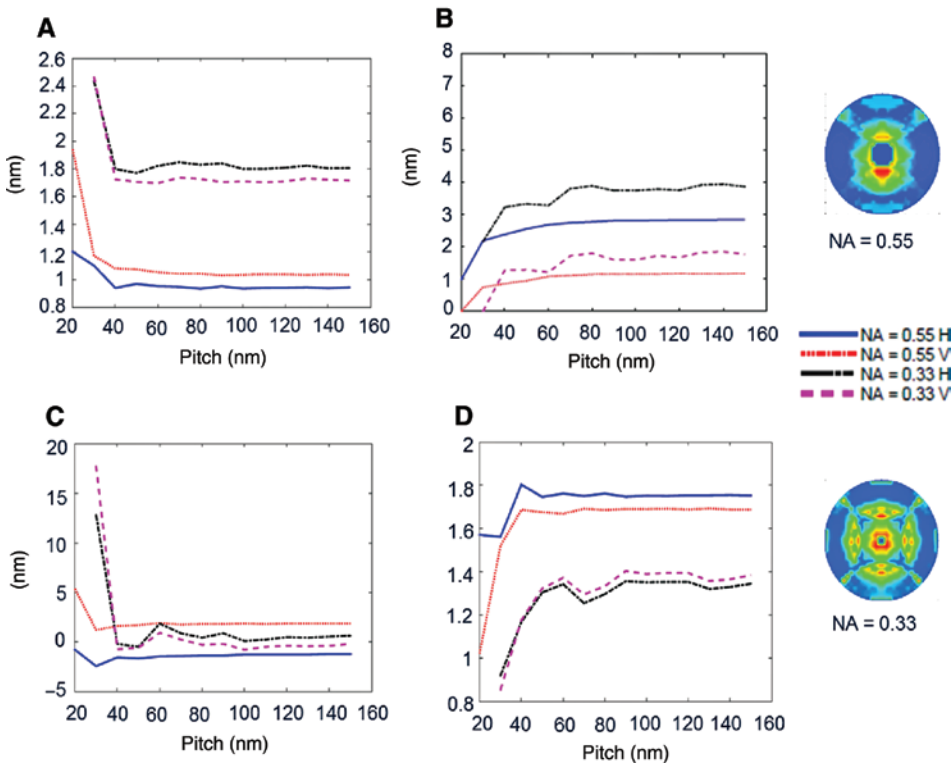
Figure 3: Comparison of CDU (A), mask bias (B), best focus shift (C), and NILS (D) for horizontal and vertical lines. We used ASML Brion's Tachyon SMO to do source and mask co-optimization without introducing SRAFs. For a fair comparison of the mask bias, both NA cases are anchored at the densest respective vertical pitch without any anchor bias.

NILS. For the 0.55-NA system, the SMO solution improves the horizontal NILS by 33% and the vertical NILS by 43%, and improves the horizontal CDU by 21% and the vertical CDU by 22%, and reduces the horizontal mask bias by 21% and the vertical mask bias by 55% compared with the mask-only optimization with annular illumination shown in Figure 2. Note that SMO aligns the focus center of all pitches and reduces the best focus shift to within ±2 nm for semi-isolated features. Next, we use SMO to co-optimize the pupil, mask, and clear SRAFs. Table 1 summarizes the number of SRAFs per unit cell through pitch. Figure 4A and D shows that SMO with SRAFs further reduces the CDU and increases NILS. The clear SRAFs help to reduce the mask bias especially for horizontal lines and align the best focus center for all semi-isolated features. Note that in this paper, all of the pupils are reticle-level pupils represented in the frequency domain of 1× wafer coordinates normalized to

NA. The SRAF width is approximately 20 nm on the reticle, which is extremely challenging for mask shops to manufacture, across the full field of the scanner. Table 2 summarizes the lithographic performance of NILS, CDU, mask bias, and overlapping DOF for different experimental settings for the 0.55-NA system. The values are averaged through pitch. The SMO pupil improves all of the above lithography metrics. The pupil from source mask co-optimization with SRAF further reduces CDU and reduces mask bias and improves overlapping DOF by 18% compared with the SMO no-SRAF case. Note that to make a fair comparison of proximity correction bias values, the dose anchor is fixed. Therefore, we exclude the anchor when reporting overlapping DOF. Table 2 clearly demonstrates that SRAFs can effectively enlarge the overlapping process window, which is beneficial for chip makers in a high-volume manufacturing (HVM) environment.

Table 1: The number of SRAFs added to the line-space main pattern per unit cell.

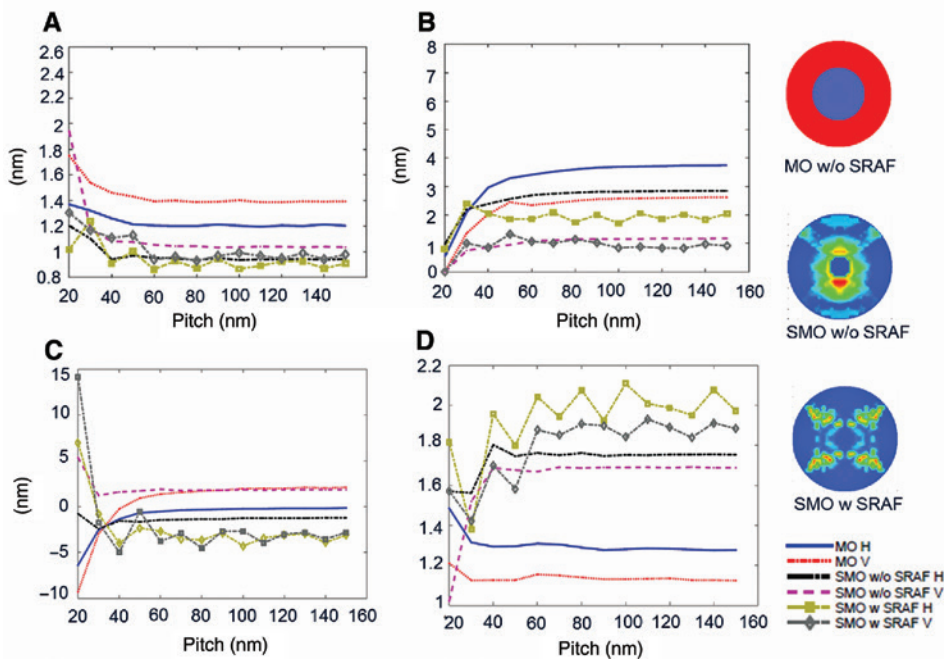| Pitch (nm)	30	40	50	60	70	80	90	100	110	120	130	140	150
Horizontal	0	1	1	2	2	3	2	4	4	2	2	4	2
Vertical	0	1	1	2	2	3	4	2	4	4	2	4	4

Figure 4: Comparison of (A) CDU, (B) mask bias, (C) best focus shift, and (D) NILS for horizontal and vertical lines for the 0.55 NA system. Here, we use ASML Brion's Tachyon software to perform OPC (mask-only optimization) without SRAF (annular source), SMO without SRAF, and SMO with SRAF.

Table 2: Summary of NILS, CDU, mask bias, and overlapping DOF for different configurations of the 0.55-NA system.

	NILS	CDU (nm)	Mask bias (nm)	Overlapping DOF (nm) at 10% EL (excluding anchor)
MO (w/o SRAF) H	1.30	1.23	3.25	10
MO (w/o SRAF) V	1.14	1.43	2.23	
SMO (w/o SRAF)H	1.73	0.97	2.58	34.8
SMO (w/o SRAF) V	1.63	1.11	1.00	
SMO (w SRAF) H	1.93	0.94	1.87	41
SMO (w SRAF) V	1.79	1.02	0.9	

The values are averaged through pitch. The SMO pupil improves all of the above lithography metrics. The pupil co-optimized with SRAF further increases NILS and reduces CDU and reduces mask bias and improves overlapping DOF by 18% compared with the SMO no-SRAF case.

3 The need for 'innovative' assist features in an EUV high-NA anamorphic system

SRAFs were introduced by Chen as an optical proximity correction technique to improve the depth of focus [9] and the overlapping process window. The size of the SRAFs is a function of wavelength and NA. As wavelength decreases and NA increases, the SRAF width needs to be reduced in order to remain sub-resolution. Kang introduced the EUV bright field symmetric attenuated SRAF and observed a 'process window tilt with middle scatter bar at 80 nm, 100 nm, 120 nm' (cf. Figure 8, Ref. [10]), but did not describe how to optimize attenuated SRAFs [10]. As design rules scale down to 20-nm pitch, EUV high-NA with very small SRAFs (≤20 nm on the reticle) are needed to meet sub-5-nm design rules, yet such small SRAFs with very high aspect ratios are very challenging to fabricate with good control across the full reticle. We propose an innovative SRAF design that enables effective optical proximity correction and improve mask manufacturability across the full scanner field.

We develop a methodology to optimize attenuated SRAFs that circumvents the challenge of fabricating extremely small clear SRAFs. To improve manufacturability, we introduce a third tone dedicated specifically for attenuated SRAFs. For dark-field masks, this third tone (attenuated SRAFs) reduces the optical weighting for light diffracted by the SRAFs. In order to match the same optical response as clear SRAFs, the width of the attenuated SRAF is increased, compensating for the energy loss as light goes through the absorber. Figure 5A shows a typical EUV reticle blank; the substrate is a low-thermal expansion material (LTEM). On the substrate, an EUV reflective multi-layer (ML) is coated. The ML needs to be covered by a capping layer to prevent any unexpected
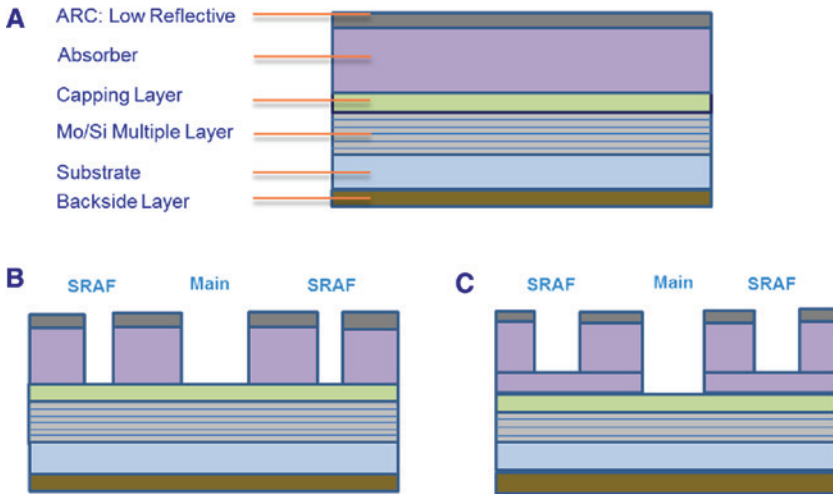
Figure 5: (A) A typical EUV reticle film stack. (B) Diagram of a clear SRAF dark-field mask. Note that in the diagram, the capping layer, which served as an etch stop is slightly etched. (C) Diagram of an attenuated SRAF dark-field mask.

oxidation. The capping layer also serves as an etch stop during the absorber etching process. Figure 5B and C illustrates reticle cross sections for clear SRAFs and attenuated SRAFs. To achieve the equivalent optical response, the absorber layer of the attenuated SRAF is not etched through to the capping layer, and the SRAF width is increased. The fabrication process steps are illustrated in Figure 6.

3.1 Asymmetric assist features

An EUV reticle typically uses a Ta-based absorber deposited on a Bragg reflector composed of 40- to 50-molybdenum/silicon (Mo/Si) multilayer stacks, which all together introduce very strong mask topology effects. Furthermore, the EUV scanner uses reflective optics with an oblique incident angle of the chief ray. Hence, the non-telecentricity of EUV optics on the reticle side results in a tilted phase front. Erdman et al. have demonstrated that mask 3D effects and non-telecentricity introduce significant quadratic and asymmetric phase responses for both small-angle and large-angle poles to a 1D horizontal line-space grating (cf. Figure 8), while the phase response from a DUV system is flat and symmetrically balanced [11]. Finders et al. also reported the same findings [12]. Figure 7 shows a diagram of the mask topography and the projection pupil for an EUV lithography system. Hsu et al. introduced the concept of asymmetric SRAFs placed beside the main features to correct the Bossung tilt and best focus shift caused by the phase error [5]. Asymmetric assist features introduce extra phase among diffraction orders to balance the phase deviations caused by oblique incidence and mask 3D effects. In an anamorphic system,
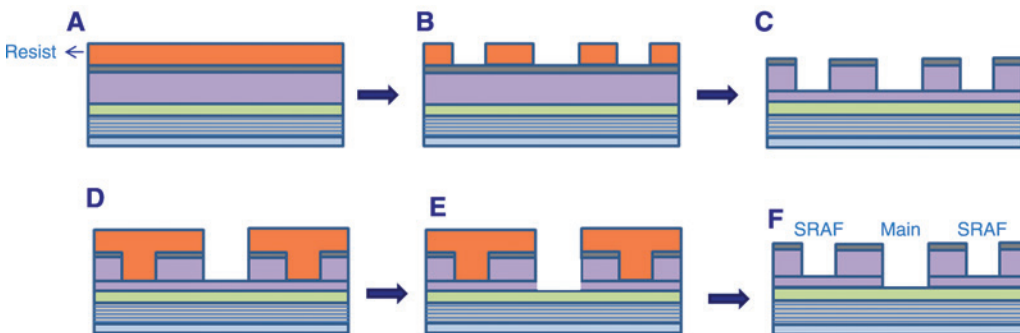

Figure 6: (A)–(F) Process steps for fabricating attenuated SRAF dark-field masks. (A) First resist coating, (B) First development, (C) First etch: main and SRAF, (D) Second resist coating and development to open the main feature, (E)Etch to thin down the main feature thickness to the capping layer and (F) Second etch.
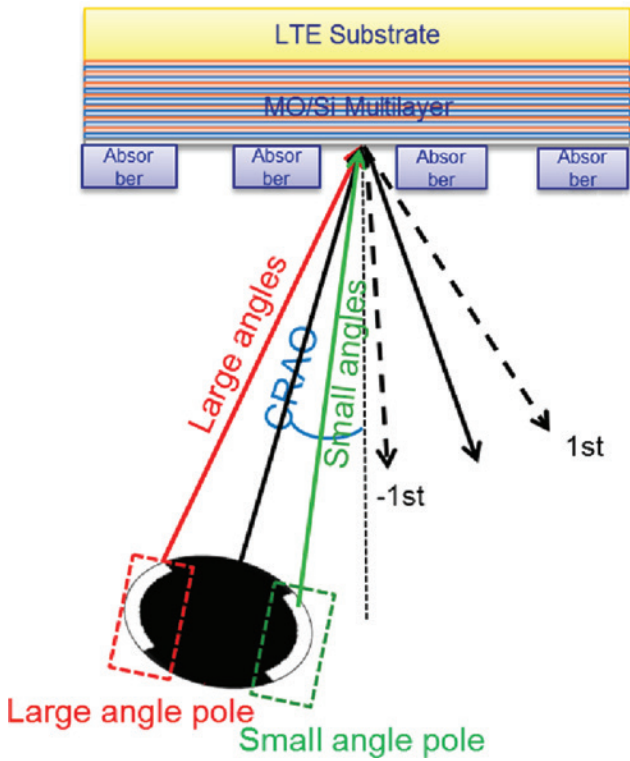
Figure 7: Schematic description of mask topography and angles of incidence for EUVL at 13.5 nm wavelength. CRAO is the chief ray angle at object side.

the demagnification is double in the scanning direction so the horizontal features suffer less mask 3D effect than the vertical features; however, we find that asymmetric clear SRAFs are still very effective in correcting Bossung tilt.

Figure 8B shows that, for horizontal lines-spaces, with the target CD = 11 nm and pitch = 70 nm, both EL and DOF improve with symmetric assist features, but Bossung tilt and best focus shifts are clearly observable. We use the same SMO-optimized pupil for 1D line-space through pitch (cf. Figure 4). To demonstrate the effect of asymmetric assist features used to balance the phase error, we placed SRAFs asymmetrically beside the main features and performed rigorous simulations to check the Bossung curves. Hyperlith program (Panoramic Technology Inc., San Jose, CA, USA) is used for these rigorous simulations. Figure 8C shows that Bossung tilt is corrected, and DOF increases from 47 nm to 63 nm at 10% EL – a 33% DOF improvement.

Next, we run rigorous simulations on vertical lines with 4× demagnification. In this configuration, projection of the chief ray on the reticle is along the direction of lines on the center slit. Therefore, there is no shadow effect from the incident wave. Figure 9 summarizes the simulation results of vertical line-space with mask CD = 11 nm pitch = 70 nm. Figure 9A shows that without SRAFs, the DOF is poor, and the Bossungs are tilted. In Figure 9B,
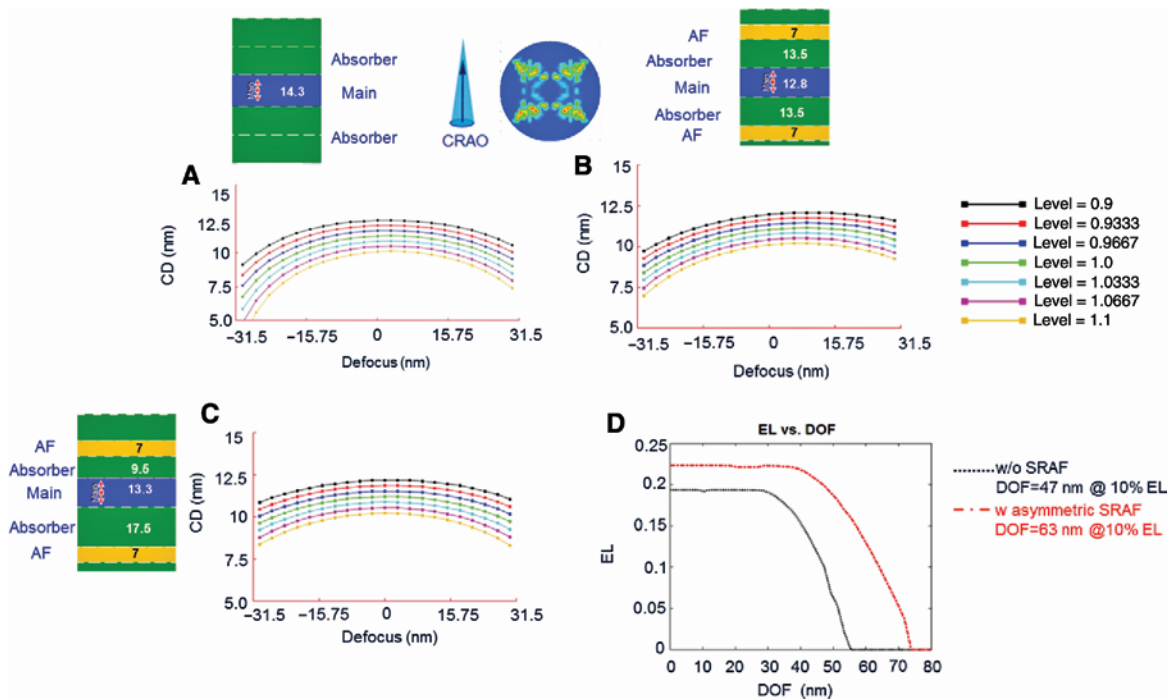

Figure 8: Horizontal line-space mask CD = 11 nm, pitch = 70 nm rigorous simulation Bossung curves with and without assist features. (A) Without assist features. The level on the legend is the dose for a given Bossung. (B) Inserting two 7-nm symmetric assist features increases the Bossung tilt. (C) Introducing asymmetric assist features effectively counteract the Bossung tilt. (D) Exposure latitude (EL) vs. depth of focus (DOF). The dose is anchored by the CD = 11 nm, pitch = 20 nm vertical lines.
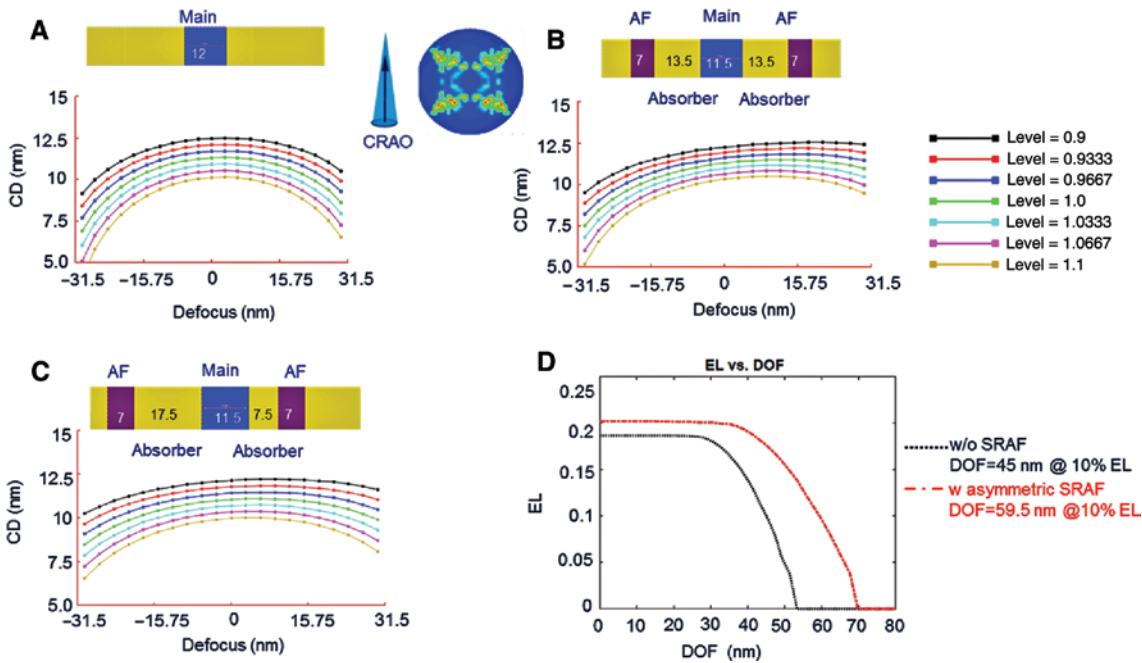
Figure 9: Vertical line-space mask CD = 11 nm, pitch = 70 nm rigorous simulation Bossung curves with and without assist features. (A) Without assist features. The level on the legend is the dose for a given Bossung. (B) Inserting a 7-nm width symmetric assist features increases the Bossung tilt. (C) Asymmetric assist features effectively counteract the Bossung tilt. (D) EL vs. DOF. The dose is anchored by the CD = 11 nm, pitch = 20 nm vertical lines.

when symmetric SRAFs are added on both sides of the main features, the Bossung tilt is clearly observed. This means that the Bossung tilt is related more to the mask 3D effects rather than the incident light direction. It has been demonstrated that an extra phase term is accumulated when light travels through the absorber trench of SRAFs compared to the main features and accounts for the Bossung tilt that is observed in simulation [13]. Figure 9C shows that asymmetric assist features are able to correct the Bossung tilt and increase DOF from 45 nm to 59.5 nm at 10% EL – a 32% DOF improvement.

3.2 Fourier analysis of attenuated assist features

Section 3.1 demonstrates that asymmetric clear SRAFs can effectively correct the Bossung tilt and improve the DOF. A 7-nm SRAF width at 1× wafer scale (28 nm on reticle) is used in the study. The current 2015 ITRS roadmap specifies the minimum on-reticle feature size to be 32 nm. The 28-nm SRAFs, therefore, cannot be reliably manufactured across a 6″ reticle. We need a solution to apply the SRAFs for EUV high-NA imaging. Here, we propose the use of
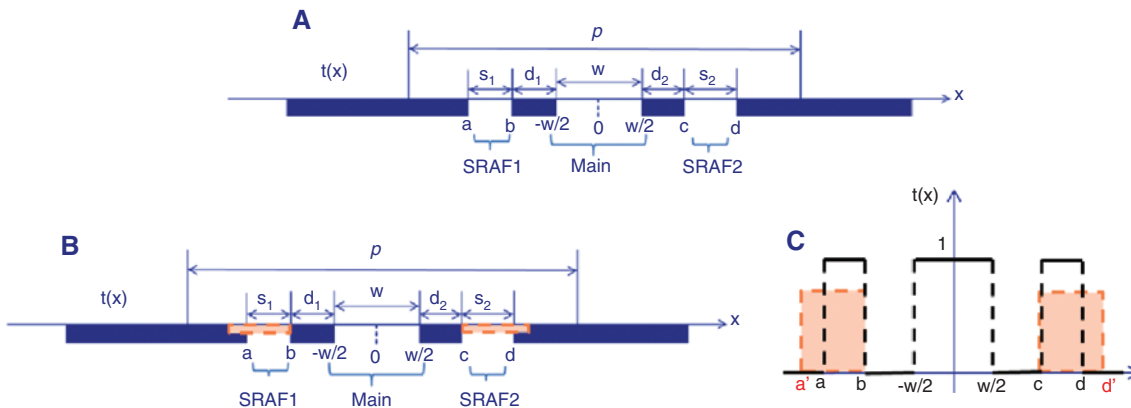

Figure 10: A dark-field mask with SRAFs and a main feature. (A) Cross-sectional view of a clear SRAF dark-field mask. (B) Cross-sectional view of an attenuated SRAF dark-field mask. (C) Transmittance t(x) comparison of clear and attenuated SRAFs for a dark-field mask.

attenuated SRAFs, which have a larger width, but maintain the same optical effect as the 28-nm clear SRAFs in the dark-field mask. To develop a method for modifying the attenuation and width of the SRAFs, we first perform a Fourier analysis on a Kirchhoff mask to match the attenuated and clear SRAFs as shown in Figure 10.

The electric field component of the diffraction field T_m for clear SRAFs is [5]:

$$T_m(f_x) = \frac{\sin \pi f_x w}{\pi f_x}$$
$$+ \frac{1}{\pi f_x}\left[\cos(\pi f_x \Delta d_1)\sin(\pi f_x s_1) + \cos(\pi f_x \Delta d_2)\sin(\pi f_x s_2)\right]$$
$$- \frac{i}{\pi f_x}\left[\sin(\pi f_x \Delta d_1)\sin(\pi f_x s_1) + \sin(\pi f_x \Delta d_2)\sin(\pi f_x s_2)\right] \quad (3)$$

We define $s_1 = b - a$; $\Delta d_1 = b + a$; $s_2 = d - c$; $\Delta d_2 = d + c$.

The electric field of the diffraction pattern T_m' for attenuated SRAFs is:

$$T_m'(f_x) = \frac{\sin \pi f_x w}{\pi f_x}$$
$$+ \frac{1}{\pi f_x}\left[t_1 \cos \pi f_x(\Delta d_1 - \Delta s_1)\sin \pi f_x(s_1 + \Delta s_1)\right.$$
$$\left. + t_2 \cos \pi f_x(\Delta d_2 + \Delta s_2)\sin \pi f_x(s_2 + \Delta s_2)\right]$$
$$- \frac{i}{\pi f_x}\left[t_1 \sin \pi f_x(\Delta d_1 - \Delta s_1)\sin \pi f_x(s_1 + \Delta s_1)\right.$$
$$\left. + t_2 \sin \pi f_x(\Delta d_2 + \Delta s_2)\sin \pi f_x(s_2 + \Delta s_2)\right] \quad (4)$$

We define the attenuated SRAF total bias Δs_1 and Δs_2, where $a' - a = -\Delta s_1$, $d' - d = \Delta s_2$. The variables t_1 and t_2 are the transmittance through the attenuated SRAFs and are real numbers. As the real part of the refractive index of the absorber, TaBN is 0.95, which is very close to the refractive index of vacuum. It is safe to ignore the phase accumulation through the absorber of the attenuated SRAFs. To help develop the following derivation, we introduce a dummy variable A_1 (attenuation of SRAF1) and let $A_1 = 1 - t_1$. For SRAF2, we introduce the attenuation A_2 and let $A_2 = 1 - t_2$, then perform Taylor expansion on equation (4) and keep the main, first-order, and partial second-order small items. We represent the real part of T_m as R_1, the imaginary part of T_m as I_1, the extra term in the real part of T_m' as R_2, and the extra term in the imaginary part of T_m' as I_2. Then, T_m' is written as:

$$T_m' = R_1 + R_2 + i(I_1 + I_2) \quad (5)$$

$$\text{and } T_m = R_1 + iI_1 \quad (6)$$

Here, we simplify $T_m(f_x)$ as T_m and $T_m'(f_x)$ as T_m', and

$$R_1 = \frac{\sin \pi w f_x}{\pi f_x}$$
$$+ \frac{1}{\pi f_x}\left[\cos(\pi f_x \Delta d_1)\sin(\pi f_x s_1) + \cos(\pi f_x \Delta d_2)\sin(\pi f_x s_2)\right] \quad (7)$$

$$R_2 = \frac{1}{\pi f_x}\begin{bmatrix} -A_1 \cos(\pi f_x \Delta d_1)\sin(\pi f_x s_1) \\ +\pi f_x \Delta s_1 \sin(\pi f_x \Delta d_1)\sin(\pi f_x s_1) \\ +\pi f_x \Delta s_1 \cos(\pi f_x \Delta d_1)\cos(\pi f_x s_1) \\ -A_2 \cos(\pi f_x \Delta d_2)\sin(\pi f_x s_2) \\ -\pi f_x \Delta s_2 \sin(\pi f_x \Delta d_2)\sin(\pi f_x s_2) \\ +\pi f_x \Delta s_2 \cos(\pi f_x \Delta d_2)\cos(\pi f_x s_2) \\ -A_1 \pi f_x \Delta s_1 \sin(\pi f_x \Delta d_1)\sin(\pi f_x s_1) \\ -A_1 \pi f_x \Delta s_1 \cos(\pi f_x \Delta d_1)\cos(\pi f_x s_1) \\ +A_2 \pi f_x \Delta s_2 \sin(\pi f_x \Delta d_2)\sin(\pi f_x s_2) \\ -A_2 \pi f_x \Delta s_2 \cos(\pi f_x \Delta d_2)\cos(\pi f_x s_2) \end{bmatrix} \quad (8)$$

$$I_1 = -\frac{1}{\pi f_x}\left[\sin(\pi f_x \Delta d_1)\sin(\pi f_x s_1) + \sin(\pi f_x \Delta d_2)\sin(\pi f_x s_2)\right] \quad (9)$$

$$I_2 = -\frac{1}{\pi f_x}\begin{bmatrix} -A_1 \sin(\pi f_x \Delta d_1)\sin(\pi f_x s_1) \\ +\pi f_x \Delta s_1 \sin(\pi f_x \Delta d_1)\cos(\pi f_x s_1) \\ -\pi f_x \Delta s_1 \cos(\pi f_x \Delta d_1)\sin(\pi f_x s_1) \\ -A_2 \sin(\pi f_x \Delta d_2)\sin(\pi f_x s_2) \\ +\pi f_x \Delta s_2 \sin(\pi f_x \Delta d_2)\cos(\pi f_x s_2) \\ +\pi f_x \Delta s_2 \cos(\pi f_x \Delta d_2)\sin(\pi f_x s_2) \\ -A_1 \pi f_x \Delta s_1 \sin(\pi f_x \Delta d_1)\cos(\pi f_x s_1) \\ +A_1 \pi f_x \Delta s_1 \cos(\pi f_x \Delta d_1)\sin(\pi f_x s_1) \\ -A_2 \pi f_x \Delta s_2 \sin(\pi f_x \Delta d_2)\cos(\pi f_x s_2) \\ -A_2 \pi f_x \Delta s_2 \cos(\pi f_x \Delta d_2)\sin(\pi f_x s_2) \end{bmatrix} \quad (10)$$

The electric field at wafer level can be approximated as $t_m = F^{-1}\{P \cdot T_m\} = \int_{-\infty}^{+\infty} P \cdot T_m(f_x) \cdot e^{i2\pi f_x x}df_x = \int_{-f_c}^{f_c} T_m(f_x) \cdot e^{i2\pi f_x x}df_x$ for clear SRAFs. Here, P is the pupil function, and f_c is the cutoff frequency of the optical system. For a periodic line-space pattern, the Fourier spectra are discrete, so we can write the aerial image as:

$$t_m = \sum_{n=-n_c}^{n_c} T_m(f_n) \cdot e^{i2\pi f_n x} \quad (11)$$

where n_c is the cutoff diffraction order for the optical system. At the center location ($x = 0$) of the aerial image, equation (11) reduces to:

$$t_m = \sum_{n=-n_c}^{n_c} T_m(f_n) \tag{12}$$

In the following derivation (cf. Figure 7), we use a y dipole, where L and S represent the large-angle and small-angle poles of the pupil. To match the aerial image at the center location before and after SRAF attenuation, we need to ensure that the total energy transmitted through a clear SRAF and an attenuated SRAF are equal.

$$\left|t_{mL}\right|^2 + \left|t_{mS}\right|^2 = \left|t_{mL}{'}\right|^2 + \left|t_{mS}{'}\right|^2 \tag{13}$$

where t_{mL}, t_{mS}, are the electric field from the clear SRAF mask, $t_{mL}{'}$, $t_{mS}{'}$ are the electric field from the attenuated SRAF mask, which are represented as:

$$t_{mL} = \sum_{n=-n_{cL}}^{n_{cL}} R_1 + iI_1 = R_{1L} + iI_{1L} \tag{14}$$

$$t_{mS} = \sum_{n=-n_{cS}}^{n_{cS}} R_1 + iI_1 = R_{1S} + iI_{1S} \tag{15}$$

$$t_{mL}{'} = \sum_{n=-n_{cL}}^{n_{cL}} R_1 + R_2 + i(I_1 + I_2) = R_{1L} + R_{2L} + i(I_{1L} + I_{2L}) \tag{16}$$

$$t_{mS}{'} = \sum_{n=-n_{cS}}^{n_{cS}} R_1 + R_2 + i(I_1 + I_2) = R_{1S} + R_{2S} + i(I_{1S} + I_{2S}) \tag{17}$$

Inserting expressions (14)–(17) into equation (13), we arrive at:

$$R_{2L}{}^2 + 2R_{1L}R_{2L} + I_{2L}{}^2 + 2I_{1L}I_{2L} + R_{2S}{}^2 + 2R_{1S}R_{2S} + I_{2S}{}^2 + 2I_{1S}I_{2S} = 0 \tag{18}$$

Equation (18) is the total intensity difference through clear or attenuated SRAF. If we ignore the second-order terms, equation (18) reduces to:

$$R_{1L}R_{2L} + I_{1L}I_{2L} + R_{1S}R_{2S} + I_{1S}I_{2S} = 0 \tag{19}$$

Note that equation (19) does not have an analytical solution, so instead, we solve it numerically to find the optimum SRAF bias (Δs) and attenuation. Assign $F = R_{1L}R_{2L} + I_{1L}I_{2L} + R_{1S}R_{2S} + I_{1S}I_{2S}$ as the cost function. Using the same illumination, solving F = 0 gives the optimum bias for an attenuated SRAF such that a clear SRAF and an attenuated SRAF generate identical aerial images at center location.

If the large-angle and small-angle poles have mirror symmetry, then we have $R_{1L} = R_{1S}$, $R_{2L} = R_{2S}$, $I_{1L} = -I_{1S}$, $I_{2L} = -I_{2S}$. Equation (19) reduces to

$$F = R_{1L}R_{2L} + I_{1L}I_{2L} = 0 \tag{20}$$

It is worth pointing out that EUV-attenuated SRAFs work very differently than a DUV-attenuated phase shift mask. For the DUV, an attenuated phase shift mask is a transmissive mask. The extinction coefficient k and the absorber thickness control the attenuation. The refractive index n controls the phase. To achieve a π phase shift requires an optimum thickness. The MoSi film thickness variation changes the phase, which introduces a placement error. For the EUV-attenuated SRAFs, the attenuation is controlled by the absorber extinction coefficient k and thickness. The concept of attenuation control is the same as for DUV, but the phase is controlled by the SRAF width and the depth etched into the absorber. As the waves propagate through the SRAF trench, which is much larger than the EUV wavelength, total internal reflection controls the path of the wave propagation and, therefore, determines the phase shift of the SRAFs with respect to the main features. For the EUV-attenuated SRAFs, the absorber refractive index n is very close to that of a vacuum, and the SRAF width increase is moderate. We can, thus, consider mainly the attenuation effect. Note that the second-order Taylor expansion used in the diffraction analysis approaches an exact solution when the amount of attenuated SRAF bias is much smaller than the clear SRAF size. Therefore, in the process of optimizing the attenuated SRAF absorber thickness, we need to constrain the range of thickness for finding an optimal performance. Attenuated SRAFs with thicker absorber thickness will cause the phase difference between SRAFs and un-patterned regions to significantly deviate from π, and lead to incomplete destructive interference and lower NILS. A detailed example of the attenuated SRAF absorber thickness optimization will be covered in Section 3.3.

3.3 Attenuated assist feature case study

For a proof of concept case, we use a vertical line-space with CD = 11 nm, pitch = 70 nm, and 7-nm wide assist features on both sides of the main features. The cutoff frequencies of the system are determined by the NA of the projection optics and the central obscuration [6]. For the 1D line-space, the spatial frequencies of diffraction orders collected by the projection optics need to be within the range of equation (21):

$$\left[\frac{\sin(CRAO)}{\lambda} - \frac{NA}{Mag \cdot \lambda}, \quad \frac{\sin(CRAO)}{\lambda} - \frac{0.2NA}{Mag \cdot \lambda} \right]$$
$$\bigcup \left[\frac{\sin(CRAO)}{\lambda} + \frac{0.2NA}{Mag \cdot \lambda}, \quad \frac{\sin(CRAO)}{\lambda} + \frac{NA}{Mag \cdot \lambda} \right] \tag{21}$$

where Mag is the demagnification ratio, $NA = 0.55$, $\lambda = 13.52$ nm. For the horizontal features, $CRAO = 5.21°$ and $Mag = 8$, and for the vertical features, $CRAO = 0°$, $Mag = 4$. We set the CRAO to be $5.21°$ based on an internal study, which showed that the CRAO is not too large to cause the degradation of reflection and not too small to cause overlap between the incident and reflective cones.

The spatial frequencies of diffraction orders for the large-angle pole are determined by:

$$f_x = \frac{n}{Mag \cdot p} + \frac{NA \cdot \sigma_c}{Mag \cdot \lambda} + \frac{\sin CRAO}{\lambda} \tag{22}$$

and for the small-angle pole by:

$$f_x = \frac{n}{Mag \cdot p} - \frac{NA \cdot \sigma_c}{Mag \cdot \lambda} + \frac{\sin CRAO}{\lambda} \tag{23}$$

In equations (22) and (23), n is the diffraction order, p is the feature pitch, and the estimated $\sigma_c = 0.3$ is the center sigma of the poles in the pupil shown in Figure 8. For the 70-nm vertical pitch ($p = 70$ nm), the following diffraction orders are within the cutoff frequencies: –3rd, –2nd, 0th, +1st orders for the large-angle pole (–1st order blocked by center obscuration) and –1st, 0th, +2nd, +3rd orders for the small-angle pole (+1st order blocked by center obscuration). As we are using two point sources with equal intensities to represent the large-angle and small-angle poles, equation (20) can be numerically solved to find the SRAF bias for a given attenuation.

Using the simple relationship between absorber thickness and transmittance:

$$t = 1 - A = \exp(-2\alpha k_0 h) \tag{24}$$

where $\alpha = 0.031$ is the imaginary part of the refractive index of TaBN, $k_0 = 2\pi/\lambda$ is the propagation constant, and h is the absorber thickness of the attenuated SRAFs. For a given absorber thickness (h), we want to find the attenuation A of the SRAFs.

Note that h should be carefully chosen based on an iterative optimization process: first, check the NILS, sidelobe, and best focus center for a given thickness. If the results do not meet the criteria of NILS (>1.5), sidelobe, and best focus shift ($<10\%$ of DOF), we need to repeat the calculation for a different thickness. The optimized attenuated SRAF thickness is $h = 11.3$ nm (16% of total absorber thickness), and the transmittance through the attenuated SRAF is $t = 0.72$, and the attenuation is $A = 0.28$.

For the 1D line-space, as we have already calculated the diffraction orders collected by the projection pupil, we can use 1× demagnification for the main features and

SRAFs to do further calculation. The diffraction of a Kirchhoff mask is shift invariant for oblique angles of incidence:

$$f_x = \frac{n}{p} \tag{25}$$

For a vertical line-space with clear SRAFs, the parameters $s_1 = s_2 = 7$ nm, $w = 11.8$ nm, $d_1 = 7.5$ nm, $d_2 = 17.5$ nm, $\Delta d_1 = -w - 2d_1 - s_1 = -33.8$ nm, $\Delta d_2 = w + 2d_2 + s_2 = 53.8$ nm are used as input in equation (20). We then solve equation (20) numerically to find the SRAF bias for the given attenuation $A_1 = A_2 = 0.28$.

Next, we run rigorous simulations for both clear SRAFs and attenuated SRAFs with the SRAF bias from the solution of equation (20). To make a fair comparison of the imaging performance of clear SRAFs and attenuated SRAFs, we use the pupil in Figure 8 for all simulations. Figure 11 shows that the attenuated SRAF bias is 2.52 nm for a 7-nm clear SRAF. The SRAF width increases by 35% for vertical features, which translates into approximately a 10-nm SRAF width increase on the reticle for 4× Mag. Even though the method of calculating attenuation and SRAF bias is based on a Kirchhoff approximation, rigorous simulation results clearly show that the aerial image of attenuated SRAFs matches very well with that of clear SRAFs (cf. Figure 12A). Furthermore, a process window
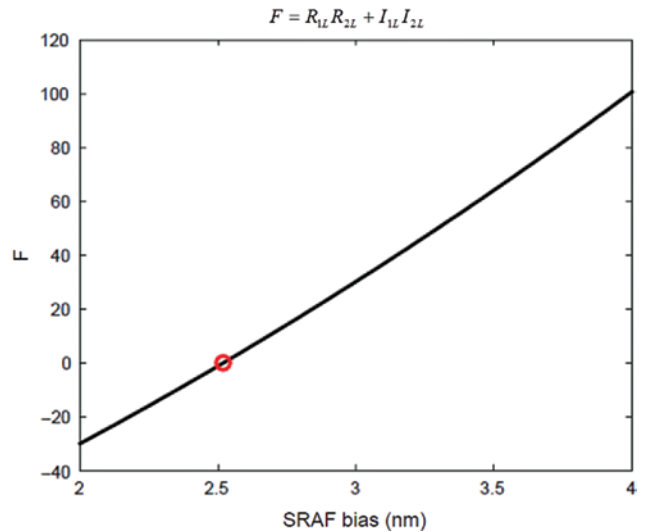

$$F = R_{1L}R_{2L} + I_{1L}I_{2L}$$

Figure 11: Numerical solution of equation (20) gives SRAF total bias $\Delta s_1 = \Delta s_2 = 2.52$ nm for a given attenuation $A_1 = A_2 = 0.28$, which is equivalent to a 11.3-nm-thick absorber for attenuated SRAFs (16% of total absorber thickness). For a vertical line-space with clear SRAFs, the parameters $s_1 = s_2 = 7$ nm, $w = 11.8$ nm, $d_1 = 7.5$ nm, $d_2 = 17.5$ nm, $\Delta d_1 = -w - 2d_1 - s_1 = -33.8$ nm, $\Delta d_2 = w + 2d_2 + s_2 = 53.8$ nm are used as input in equation (20). Here, we use F to represent $R_{1L}R_{2L} + I_{1L}I_{2L} = 0$. $F = 0$ indicates that we find the geometric settings for attenuated SRAFs so that clear SRAFs and attenuated SRAFs generate an identical aerial image at center location under the same illumination source.
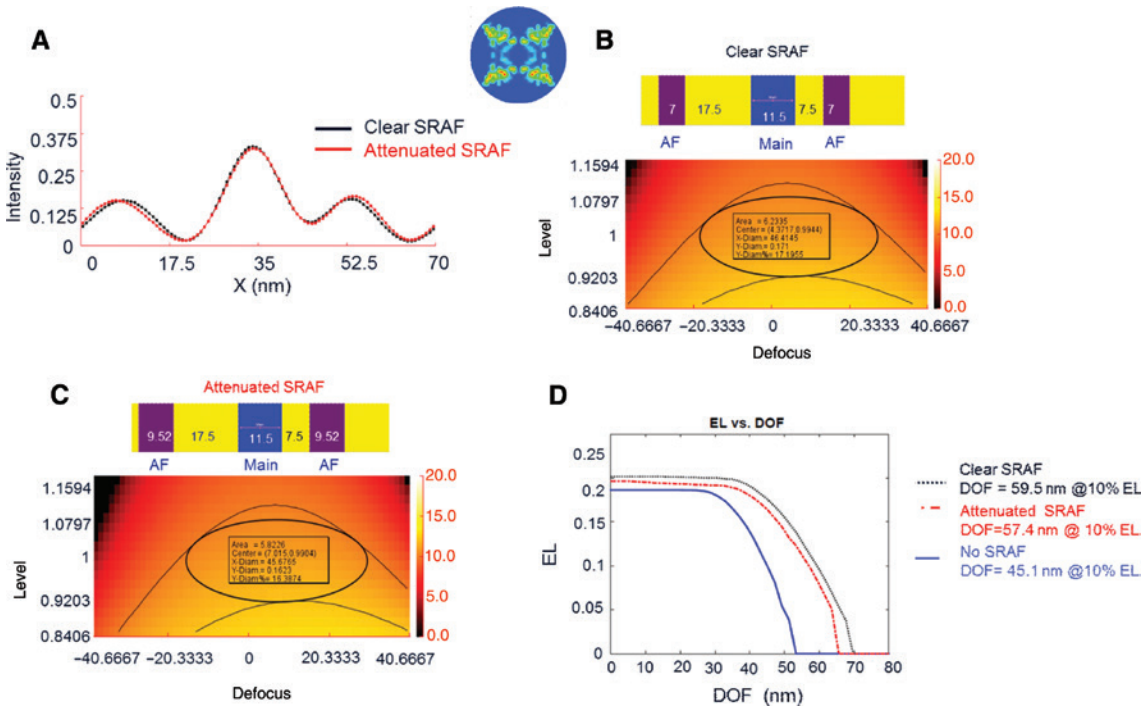
Figure 12: (A) Aerial image comparison of clear SRAFs and attenuated SRAFs from solving equation (20); the aerial image peak intensity and SRAF sidelobe shows very good agreement. (B), (C) PW analysis of clear SRAFs and attenuated SRAFs, respectively. (D) EL vs. DOF curves. Comparing the no SRAF, clear SRAF, and attenuated SRAF cases, we see good agreement between the aerial image of attenuated SRAFs and that of clear SRAFs. Process window analysis shows clear SRAFs, and attenuated SRAFs gives comparable DOF at 10% EL (59 nm vs. 57 nm). Hence, the method of optimizing attenuated SRAFs increases SRAF width, improves mask-making manufacturability, and also maintains equivalent optical performance.

analysis shows comparable DOF and EL performance (cf. Figure 12B, C). With the results in Figure 12, we have demonstrated that the method of optimizing attenuated SRAFs not only increases the SRAF width, improving mask-making manufacturability, but also maintains the necessary optical performance (cf. Figure12D).

Figure 13B and C shows how NILS and sidelobe printing vary with changes in SRAF absorber thickness and SRAF width. The SRAF thickness (%) is defined as the ratio of attenuated SRAF thickness over total absorber thickness. A thinner SRAF absorber thickness and a larger SRAF width leads to higher NILS (Figure 13B), but also suffers from a sidelobe printing issue (the white border line indicates the region where SRAF sidelobe intensity minus print threshold is larger than zero). The best solution (green dot) balances SRAF absorber thickness and SRAF width, and provides the highest possible NILS with a larger SRAF width within the mask-writing capability. We use line-space example to demonstrate the method to optimize attenuated SRAFs. To apply this method to a full chip, model-based SRAF tuning using the same principle is more effective: first, optimize the attenuated SRAF absorber thickness as the third tone, then build a tri-tone

mask 3D library to calculate the complex scattering coefficient, then finally solve the inverse problem using gradient-based optimization to obtain the optimum SRAF placement. Meanwhile, apply a sidelobe penalty to guard against sidelobe printing and an MRC penalty to guard against MRC.

Optimizing attenuated assist feature placement and width offers a powerful knob to control Bossung tilt and adjust the best focus center. The flow is as follows: first optimize the mask with clear SRAFs, then optimize the SRAF absorber thickness under constraints of NILS, sidelobe, and best focus shift, and finally apply the attenuated SRAF method. Figure 14 shows the final optimized masks for horizontal and vertical pitches 50 nm, 60 nm, and 70 nm. In this part of the study, the total absorber thickness is 70 nm. We further perform a batch simulation by varying the absorber SRAF thickness % from 0 (clear SRAF) to 40 (28 nm absorber height). For 16% absorber thickness, the foci center are within ±2.7 nm, which is well aligned for all pitches. Also, the best focus shift varies as a continuous function of attenuated SRAF absorber thickness. This is due to the various phase accumulation through the attenuated absorber, while
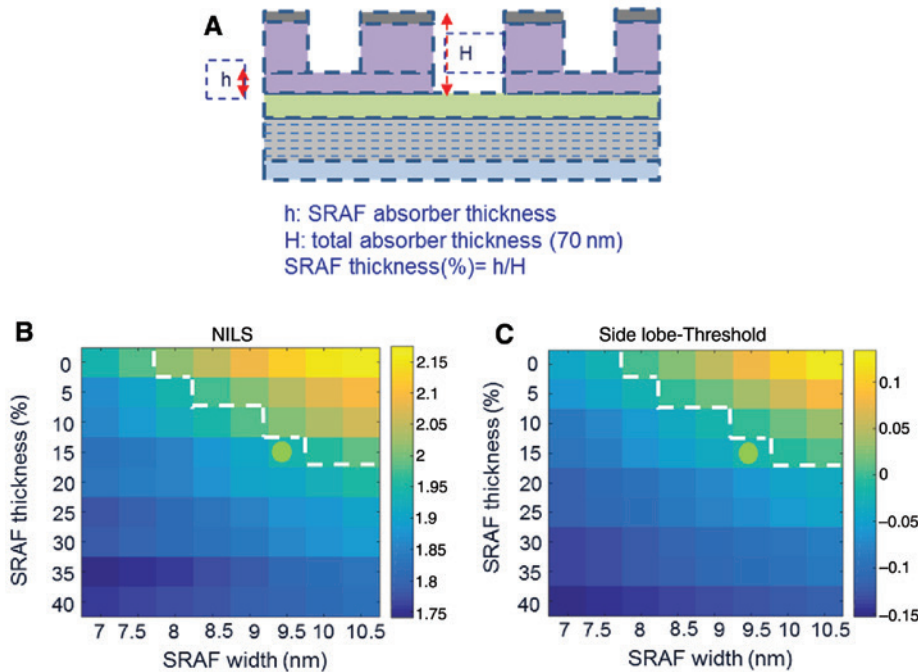
Figure 13: (A) Diagram showing the definition of SRAF thickness as a percentage based on the ratio of attenuated SRAF thickness over total absorber thickness. (B), (C) NILS and 'sidelobe-threshold' value as a function of SRAF thickness (%) and SRAF width. 'Sidelobe-Threshold' >0 will cause unwanted slidelobe printing. The region above the white dashed line shows where sidelobe printing occurs. The green dot marks the optimum configuration of attenuated SRAF for vertical 70-nm pitch lines. The best solution balances SRAF absorber thickness and SRAF width and provides the highest possible NILS at a larger SRAF width that improves the SRAF manufacturability.
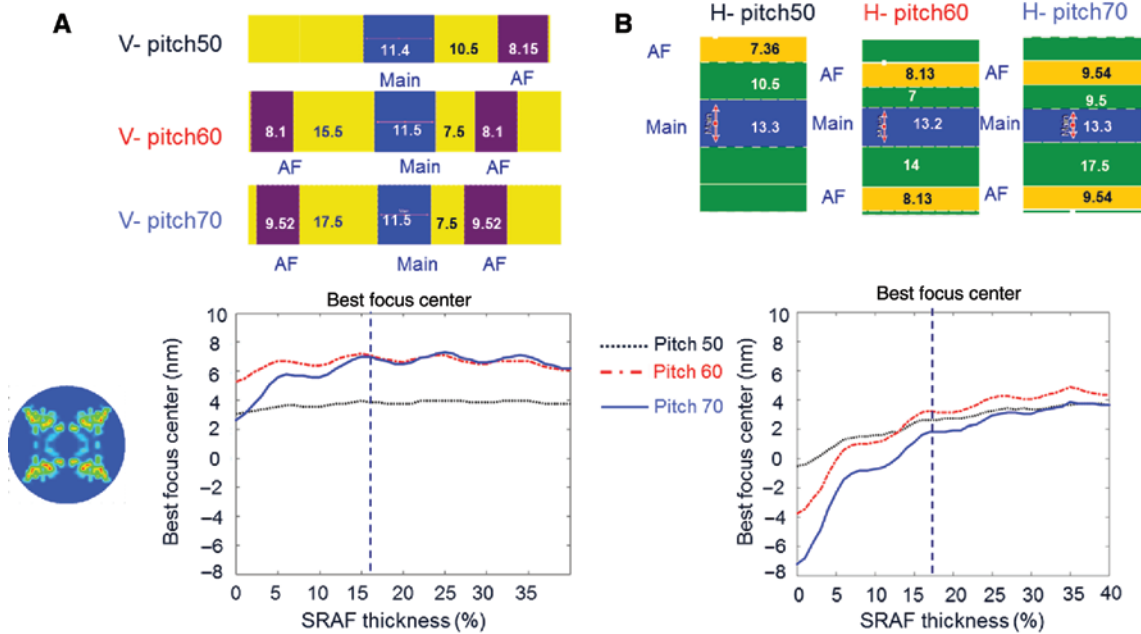

Figure 14: The best focus center vs. SRAF absorber thickness (%) for: (A) vertical pitch and (B) horizontal pitch. We perform batch simulations by varying the absorber SRAF thickness from 0 to 40%. For 16% absorber thickness, foci center are within ±2.7 nm, well aligned for all pitches. Also, the best focus shift varies as a continuous function of attenuated SRAF absorber thickness. This is due to the various phase accumulation through the attenuated absorber.

the light is traveling through the trench and down to the multilayer Bragg reflector mirror and then backscattering through the narrow gap. We further compare the overlapping process window for horizontal and vertical 50-nm, 60-nm, and 70-nm pitches among no SRAF, clear SRAF, and attenuated SRAF treatments with the same illumination as shown in Figure 15. Both clear SRAFs and attenuated SRAFs improve the DOF approximately 14% and 15% (Figure 15). The best focus of the anchor (vertical pitch 20 nm lines) is set as the focus center and used as a reference for calculating the best focus shift of other features. For vertical pitches 60 nm and 70 nm, the best focus center is shifted due to the residual phase error, which causes best focus misalignment with the anchor.

4 MEF and mask-manufacturing rule check (MRC)

Typically, electronic design automation (EDA) tools represent the circuit layout at 1× wafer scale. To tape out a design for an anamorphic optical system, the OPC mask should be asymmetrically scaled by 8× for the horizontal features and by 4× for the vertical features during reticle data preparation. In order to accurately account for the mask 3D effect, the actual shapes and orientations of the features need to be properly modified to produce correct polygon shapes. To illustrate the difference for 4× by 8× anamorphic reticle, Figure 16 shows that the 45° tilted rectangular target are stretched by 8× in the scanning direction and by 4× in the perpendicular direction. As a result, the reticle is distorted, and the corresponding tilt angle is 63.43° for long and short edges. Therefore, we need a new metrology mapping system from design data to reticle for CD gauges (cf. Figure 16C). And the angle on reticle and the angle on target is related by $\tan(\theta_{reticle}) = 2\tan(\theta_{target})$. In addition, for fast M3D modeling and OPC, we need to build a mask 3D library with the target-to-reticle mapping for CD and tilt angles.

As the reticle writer grid and error is isomorphic, for an anamorphic system, the horizontal features are less sensitive to the mask-writing errors than the vertical features; therefore, in SMO, horizontal features require looser criteria in terms of mask-bias perturbation for MEF minimization. Thus, it makes sense to perform MEF optimization using two different criteria. For angled features, there
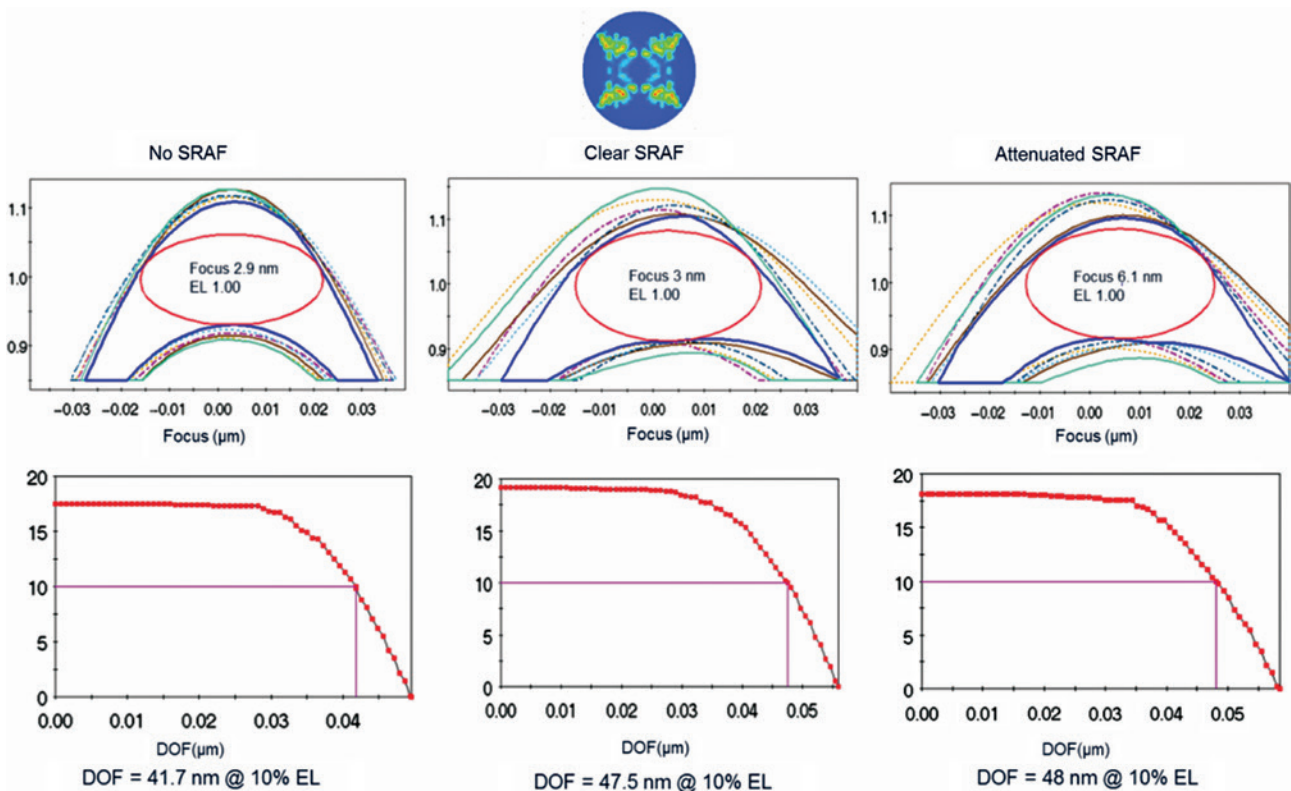

Figure 15: The overlapping process window for no SRAFs, clear SRAFs, and attenuated SRAFs, which are simulated using the mask geometries shown in Figure 14. All of the simulations use the same illumination source. Both clear SRAFs and attenuated SRAFs improve the DOF approximately 14% and 15%.
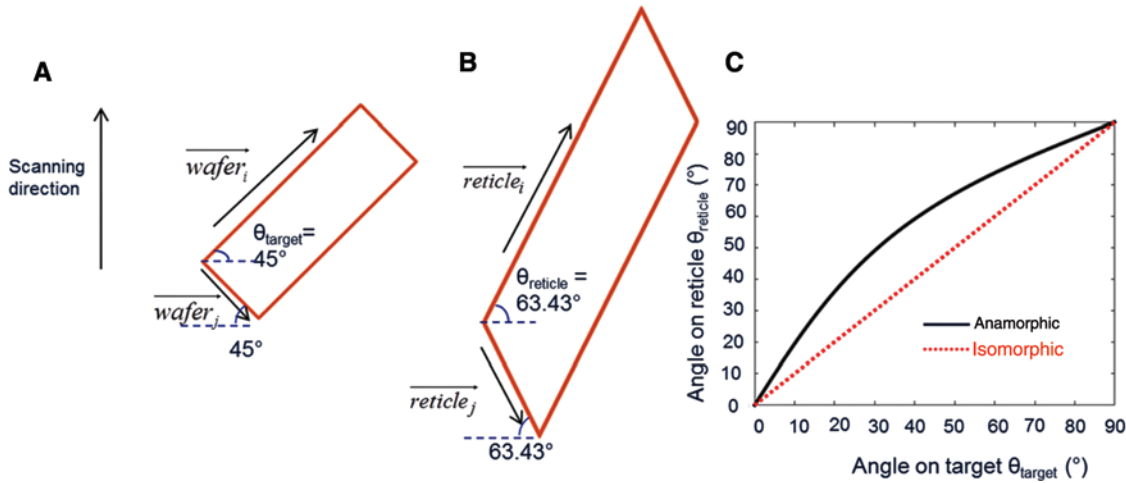
Figure 16: Illustration of a tilted pattern in the (A) 'target' and (B) 'reticle' levels. (C) For angled feature in a 4× by 8× anamorphic system, the relationship between the angle on the reticle and angle on the target is no longer linear as it is the isomorphic system.

are no definitions of horizontal and vertical directions. An alternative solution to calculate the MEF is to apply OPC bias in the reticle plane, perform mask 3D simulation, convert the image to the 1× wafer plane, and measure the edge placement error (EPE).

4.1 Angular-dependent MEF

The MEF is defined as the change in the wafer CD from a change in the reticle CD error. The definition of MEF is:

$$\text{MEF} = \frac{\partial CD_{wafer}}{\partial CD_{reticle}/M(x,y)} \quad (26)$$

where M is the demagnification factor. For an anamorphic system, the demagnification has angular dependency; we can still use equation (26) for MEF calculation by incorporating angular-dependent demagnification.

For anamorphic systems, we need to consider the demagnification factor M to calculate the MEF and correctly link the design target and gauges on the reticle for tilted features. Figure 17A–C illustrates the mapping between target, reticle, and wafer [14]. Figure 17B shows that for an angled pattern at reticle level, there are three metrologies [CD_1, CD_2 and CL (cutline)] to quantify the $CD_{reticle}$, while in the 1× plane, we only need two metrology measurements to fully specify the dimension of an angled polygon (Figure 17A). To fully characterize the same
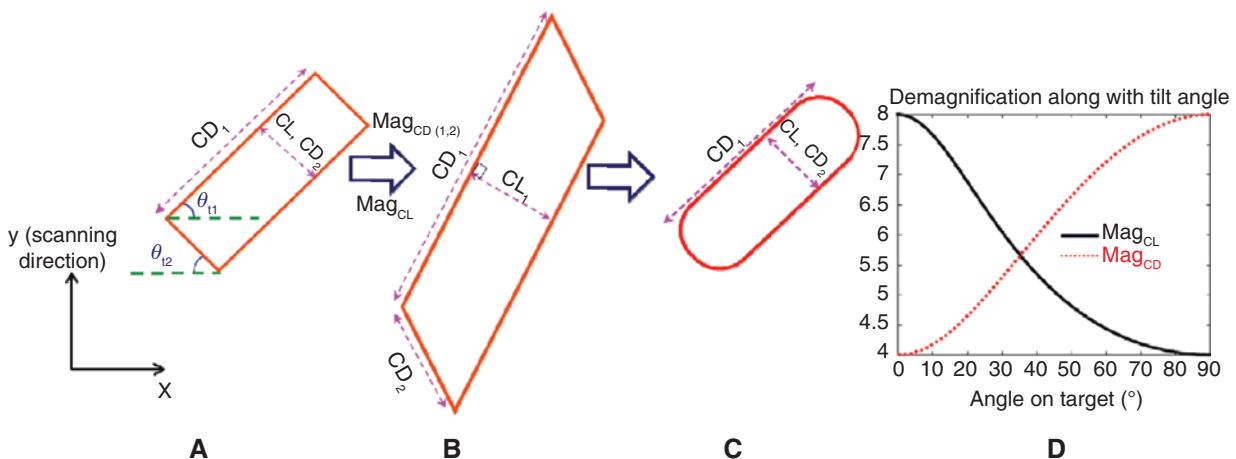

Figure 17: The mapping from design target and gauges to reticle for an angled polygon: from target (A) to reticle (B), and to wafer (C). To quantify the mask-writing error for an angled pattern at reticle level, we need three metrologies [CD_1, CD_2 and CL (cutline)], while in the 1× plane, we only need two metrology measurements to fully specify the angled polygon. (D) The demagnification varies with the angle of the target polygon.

polygon dimension after mask writing on the reticle, it needs three measurements: CD_1, CD_2, and CL. The corresponding demagnification factors for those three metrologies are calculated using geometric methods, and the general equations are written by equations (27) and (28):

$$\text{Mag}_{CD(1,2)} = M_x \sqrt{\cos^2 \theta_{t(1,2)} + \left(\frac{M_y}{M_x}\right)^2 \sin^2 \theta_{t(1,2)}} \tag{27}$$

$$\text{Mag}_{CL} = \frac{M_y}{\sqrt{\cos^2 \theta_{t1} + \left(\frac{M_y}{M_x}\right)^2 \sin^2 \theta_{t1}}} \tag{28}$$

where $M_x = 4$, $M_y = 8$, and $\theta_{t(1,2)}$ are tilt angles for the long edge and short edge with respect to the x axis, respectively. Figure 17D shows the demagnification changes with the angle of the target (the variation of $\text{Mag}_{CD(1,2)}$ and Mag_{CL} along with the angle of the target). The demagnification factor is changing between 8× and 4×. Mag for the CD of a tilted rectangular feature can be further generalized in the matrix form:

$$\begin{bmatrix} \overline{\text{reticle}_i} \\ \overline{\text{reticle}_j} \end{bmatrix} = \begin{bmatrix} \text{Mag}_i & 0 \\ 0 & \text{Mag}_j \end{bmatrix} \begin{bmatrix} \overline{\text{wafer}_i} \\ \overline{\text{wafer}_j} \end{bmatrix} \tag{29}$$

where

$$\text{Mag}_i = M_x \sqrt{\cos^2 \theta + \left(\frac{M_y}{M_x}\right)^2 \sin^2 \theta} \quad \text{and}$$

$$\text{Mag}_j = M_x \sqrt{\sin^2 \theta + \left(\frac{M_y}{M_x}\right)^2 \cos^2 \theta}; \quad \theta \text{ is the angle defined}$$

in Figure 16A. The Mag matrix can be proven using a coordinate transform. It represents the dependence of geometric coordinates on the reticle and on the wafer. Equation (29) indicates that for an anamorphic system, the demagnification of the CD has an angular dependency. Therefore, the MEF also has an angular dependency. The anamorphic MEF for any rectangular features can be generalized in an angular-dependent MEF tensor:

$$\text{MEF} = \begin{bmatrix} \dfrac{\Delta CD_{\text{wafer}_i}}{\Delta CD_{\text{reticle}_i}/\text{Mag}_i} & \dfrac{\Delta CD_{\text{wafer}_i}}{\Delta CD_{\text{reticle}_j}/\text{Mag}_i} \\ \dfrac{\Delta CD_{\text{wafer}_j}}{\Delta CD_{\text{reticle}_i}/\text{Mag}_j} & \dfrac{\Delta CD_{\text{wafer}_j}}{\Delta CD_{\text{reticle}_j}/\text{Mag}_j} \end{bmatrix} \tag{30}$$

Actually, independent of anamorphic or isomorphic imaging, for 2D contact holes, there is a coupled electromagnetic response by light excitation on the neighboring edges. Specifically, the coupling factor quantifies the influence of polygon edge error at reticle level on the neighboring wafer edges. Thus, the MEF is best expressed in the tensor form. It should be noted that there are no off diagonal terms in the Mag matrix (equation 29), so in the tensor MEF definition, we only consider the Mag in the same direction with the ΔCD_{wafer} coordinate (equation 30).

4.2 MRC consideration

From a reticle-manufacturing specification point of view, the reticle MRC is more relaxed in the 8× (scanning) direction, as the line-space and corner-to-corner dimensions are twice as large as for features in the 4× direction. Consequently, the 8× direction has more space for OPC bias correction and placing more SRAFs and/or wider SRAFs. Figure 18A is the optimized mask at 1×, and Figure 18B illustrates the SRAF placement for an anamorphic mask, which allows more SRAFs to be inserted in the y direction. Figure 18C is a block layer at 1× with touching corners, which is problematic for applying OPC. Figure 18D is the modified corner treatment for OPC, and Figure 18E is the anamorphic reticle (4×, 8×).

In summary, for anamorphic systems, we need to consider the angular-dependent demagnification to calculate the MEF tensor for 2D features. In fact, the MEF tensor should be used independent of anamorphic or isomorphic imaging, for 2D contact, via the type of features. For MRC constrains on reticle, as mask-writing grid is isomorphic, there is no difference in writing an anamorphic or isomorphic reticle. SMO and OPC need to consider that the 8× direction has more spacing for biasing and inserting SRAF.

5 Conclusion

In this paper, we analyze the fundamental high-NA EUV imaging advantages, the challenge of small DOF, and develop a methodology to optimize attenuated SRAFs to address that challenge. First, a high-NA system is beneficial for enhancing resolution, minimizing mask bias, and controlling CDU. Source mask optimization correctly optimizes the source, applies sub-resolution assist features, improves the contrast, and overlapping DOF for high-NA EUV lithography. Second, small SRAFs (~20 nm on the reticle) are very challenging to fabricate with good control across a full reticle. We introduce an innovative method to optimize 'attenuated SRAFs', which increases the SRAF
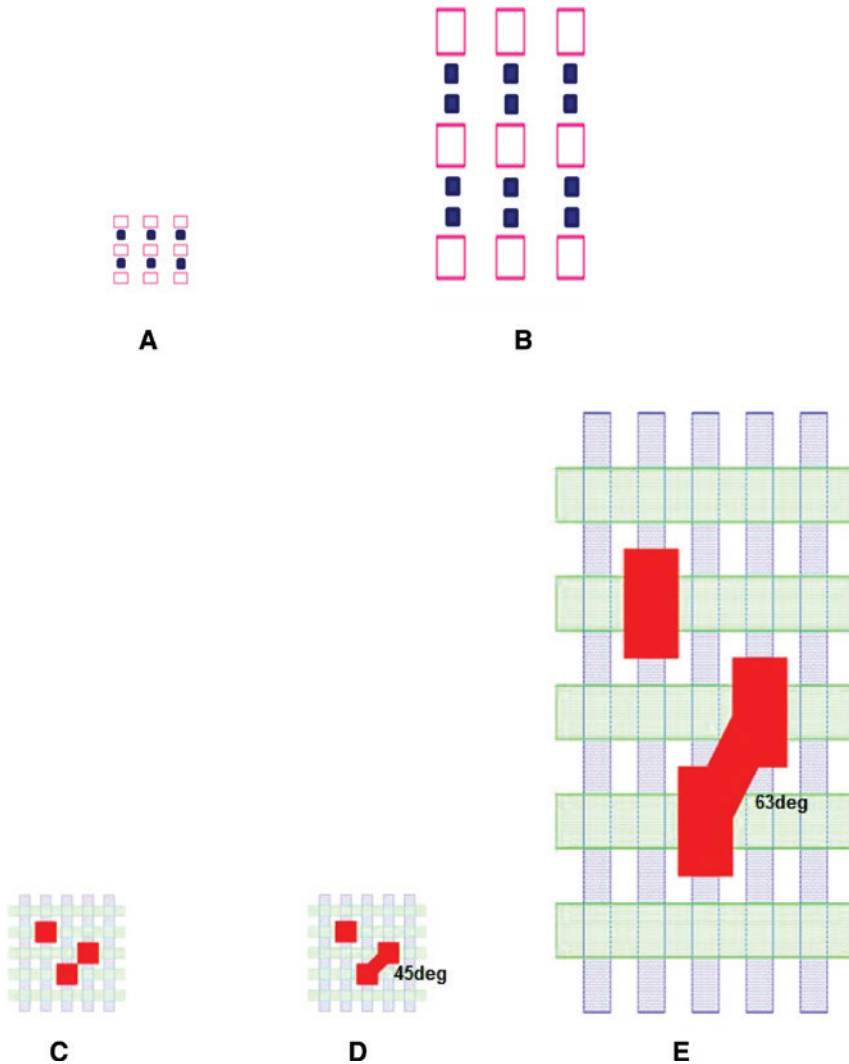
Figure 18: (A) Isomorphic via mask (1×) and (B) anamorphic reticle (4×, 8×), the SRAF placement for an anamorphic mask, which allows more SRAFs to be inserted in the space in the y direction. (C) Horizontal line space is the metal layer, red is the isomorphic block mask (1×), (D) is the block mask (1×) with modified corner treatment for OPC, and (E) is the anamorphic reticle (4×, 8×).

width to improve the SRAF manufacturability, while maintaining equivalent imaging performance. Third, we demonstrate the use of MEF tensors in an anamorphic imaging system. We also propose a redefinition of the MRC in anamorphic EUV SMO and OPC, which allows more relaxed MRC rules in the 8× scanning direction. We believe that these new computational lithography techniques can be beneficial for implementing EUV high-NA lithography for volume production.

References

[1] B. Turko, S. L. Carson, A. Lio, T. Liang, M. Phillips, et al., in 'Proc. SPIE9776, Extreme Ultraviolet (EUV) Lithography VII', vol. 977602 (2016) doi: 10.1117/12.2225014.

[2] A. Lio, in 'Proc. SPIE9776, Extreme Ultraviolet (EUV) Lithography VII', vol. 97760V (2016) doi: 10.1117/12.2225017.

[3] O. Wood, S. Raghunathan, P. Mangat, V. Philipsen, V. Luong, et al., in 'Proc. SPIE. 9422, Extreme Ultraviolet (EUV) Lithography VI', vol. 94220I (2015) doi: 10.1117/12.2085022.

[4] S. Raghunathan, G. McIntyre, G. Fenger, O. Wood, in 'Proc. SPIE8679, Extreme Ultraviolet (EUV) Lithography IV', vol. 867918 (2013) doi: 10.1117/12.2011643.

[5] S. Hsu, R. Howell, J. Jia, H.-Y. Liu, K. Gronlund, et al., EUV 'Proc. SPIE9048, Extreme Ultraviolet (EUV) Lithography VI', (2015) doi: 10.1117/12.2086074.

[6] B. Kneer, S. Migura, W. Kaiser, J. T. Neumann, J. van Schoot, in 'Proc. SPIE9422, Extreme Ultraviolet (EUV) Lithography VI', vol. 94221G (2015) doi: 10.1117/12.2175488.

[7] J. van Schoot, K. van Ingen Schenau, G. Bottiglieri, K. Troost, J. Zimmerman, et al., 'Proc. SPIE. 9776, Extreme Ultraviolet (EUV) Lithography VII', vol. 97761I (2016) doi: 10.1117/12.2220150.

[8] M. Burkhardt, A. Raghunathan, in 'Proc. SPIE9422, Extreme Ultraviolet (EUV) Lithography VI', vol. 94220X (2015) doi: 10.1117/12.2085948.

[9] J. Fung Chen, T. Laidig, K. E. Wampler, R. Caldwell, J. Vac. Sci. Technol. B 15, 2426–2433 (1997).

[10] H. Kang, in 'Proc. SPIE 7520, Lithography Asia 2009', vol. 752037 (2009) doi: 10.1117/12.849556.

[11] A. Erdman, P. Evanschitzky, J. T. Neumann, P. Gräupner, in 'Proc. SPIE 9426, Optical Microlithography XXVIII', vol. 94260H (2015) doi: 10.1117/12.2086346.

[12] J. Finders, L. Winter, T. Last, J. Micro/Nanolith. MEMS MOEMS 15, 021408 (2016). doi: 10.1117/1.JMM.15.2.021408.

[13] M. Burkhardt, G. McIntyre, R. Schlief, L. Sun, in 'Proc. SPIE 9048, Extreme Ultraviolet (EUV) Lithography V', vol. 904838 (2014) doi: 10.1117/12.2048311.

[14] D. Hsu, J. Liu, U.S. Application No. 62/322677 'Mapping of patterns between design layout and patterning device' April 14, 2016.